Hindawi
International Journal of Antennas and Propagation
Volume 2019, Article ID 1782942, 10 pages
https://doi.org/10.1155/2019/1782942

Research Article

Ionospheric Clutter Model for HF Sky-Wave Path Propagation with an FMCW Source

Xuguang Yang,[1,2] Aijun Liu,[3] Changjun Yu,[3] and Linwei Wang[3]

[1]*Department of Electronic and Information Engineering, Harbin Institute of Technology, Harbin 150001, China*
[2]*School of Information Engineering, Long Dong University, Gansu 745000, China*
[3]*Department of Information and Communication Engineering, Harbin Institute of Technology (Weihai), Weihai 264209, China*

Correspondence should be addressed to Aijun Liu; liuaijun@hit.edu.cn

Received 16 November 2018; Accepted 10 April 2019; Published 8 May 2019

Academic Editor: Shiwen Yang

A theoretical model of the sky-wave path propagation with frequency modulated continuous wave (FMCW) source for high frequency (HF) radar is proposed in this paper. Based on the modeling of pulsed source, the expression of the received electric field with an FMCW source is derived for the reflection case from the ionospheric irregularities. Subsequently, the ionospheric reflection coefficient with different phase power spectrums for vertical and oblique backscattering propagation paths is incorporated into the ionospheric clutter model. Simulation results show that the peak power of FMCW in average is lower than that of pulsed waveform. Furthermore, different incident angles and magnetic field in mid-latitude can also influence the power density of the backscattering ionospheric clutter. Finally, the data analysis results from the high frequency surface wave radar (HFSWR) and Ionosonde collected in Yellow Sea preliminarily verify the inversion of the variance of the electron density fluctuation and the vertical drift velocity of the irregularities within ionosphere.

1. Introduction

In high frequency surface wave radar (HFSWR) system, the electromagnetic wave diffracts along the curvature of the earth to detect ships and low flying aircraft targets over the horizon. Ideally, a perfect conductive plane consisting of sea surface is infinite in coverage area and thus makes transmitted wave entirely traveling along the sea surface. But if considered the affection of poor ground, the overhead nulling of the receiving pattern will shift to left, which causes the whole vertical radiation pattern gain [1]. Simulations by High Frequency Structure Simulator (HFSS) show that transmitting antenna of HFSWR radiates partial energy to elevation especially to the overhead regardless of frequency [2]. The pattern of vertically polarized antenna receiving arrays also has -8dB gain on overhead. Thus partial wave radiated upwards and reflected from the ionosphere is unavoidable. The echo arrived at the receiving antennas from various paths, which is referred to as ionospheric clutter [3, 4].

We summarize the path of ionospheric clutter in two kinds: the sky-wave path (include vertical and oblique propagation) and mixed path (via the ocean surface path), as shown in Figure 1. Simulations show that the most effective paths are the vertical path and mixed path [1]. However, the oblique sky-wave path should also exist in HFSWR system, since the attenuation of ocean path is much higher than sky path and the detection range of HFSWR can reach 400-600km. Therefore, if the ionosphere-ocean mixed path exists, the oblique propagation path (0.5 jumps, 1 jumps, etc.) should also exist. The backscattering propagation range (0.5 jumps) is far away from the vertical propagation range, but shorter than mixed propagation range.

Figure 2 shows the comparison between ionogram and RD (range Doppler) spectrum of HFSWR on 10:53 am, June 28, 2018, location: Weihai (37.5°N, 122°E), China. In the ionogram, the green points are locus of received extraordinary frequencies and their corresponding virtual height. The red points are locus of ordinary frequencies and their corresponding virtual height. We can see that the E layer is in 100-150km and the critical frequency is less than 5MHz. But the radar operating frequency is 6MHz and the ionospheric range is about 150-200km. Therefore, it should be the oblique ionospheric clutter in HFSWR.

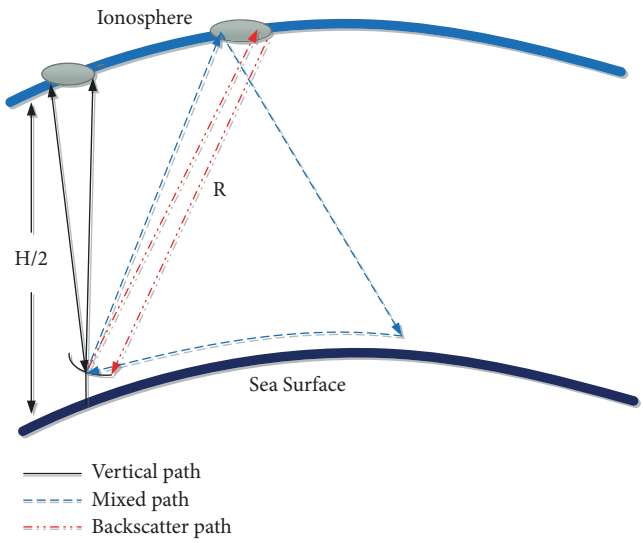

Figure 1: Propagation paths of HFSWR ionospheric clutter.

The ionospheric clutter often spread in range, Doppler, and spatial domains, leading to the masking of targets. Most of the clutter is caused by plasma density irregularities in the ionosphere under disturbed ionospheric conditions [5]. Thus it is necessary to develop a mathematic model to quantify the impact of the ionosphere. Many investigations have been made on the characterization of ionospheric clutter and suppression of ionospheric clutter [6–11]. These ionospheric clutter mitigating techniques include many complicated adaptive signal processing algorithms or additional antennas. However, these techniques benefit from a physical model based on scattering mechanism, which demonstrates how the ionospheric clutter manufactured between electromagnetic wave and irregularities caused by plasma instabilities.

Walsh et al. [12] laid a solid theoretical foundation to describe the scattering of electromagnetic waves from the ocean surface, which has been extended to model the power spectral density of mixed path propagation for pulsed radar [13] and a frequency modulated continuous wave (FMCW) radar [14]. In those models, the ionospheric reflection coefficient (IRC) is assumed as Gaussian function, which may not accord with the ionosphere physical conditions. In [15], the model of the ionospheric clutter from vertical incidence for HFSWR and Bragg backscatter in the auroral zone for over-the-horizon radar (OTHR) were developed using a geometric optic approach. Chen incorporates the particular ionospheric clutter model into Walsh's model for mixed path with an FMCW [16, 17] and vertical reflection with pulsed radar [18]. However, the case of vertical propagation for FMCW and oblique sky-wave propagation has not been considered. Since the main waveform in HFSWR system is FMCW or phase coding waveform, the vertical theoretical model with pulsed cannot be validated. In this paper, we investigate the vertical reflection with FMCW source, compared the simulation results with pulsed source and test the experimental results with Ionosonde. Besides, we derive the generalized power spectrum for backscatter sky-wave propagation (0.5 jumps) in mid-latitude.

The remaining part of the paper is organized as follows. In Section 2, the electric field equation and vertical power spectrum of FMCW source are obtained under the assumption of a continuously excited elementary vertical dipole source. The backscattering power spectrum incorporated with a phase power spectrums of ionospheric irregularities in mid-latitude is derived in Section 3. In Section 4, simulations are conducted for FMCW and compared the experimental results with Ionosonde. Conclusions are summarized in Section 5.

2. Vertical Received Power Spectrum for FMCW Source

Suppose that a dipole transmitting antenna is at coordinate $(0, 0, 0)$, the ionospheric reflecting layer is at a height of $H/2$, and the dipole image is at height of H, as shown in Figure 3. The angle of incidence is θ_i. In the case of vertical reflection, we have $\theta_i = \delta\theta$, which is the angle error of the antenna pattern. Thus the vertical incidence is a special case of oblique backscattering.

Based on image theory [13, 18], the scattered electric field equations for the backscattering ionospheric clutter at $(0, 0, 0)$ can be written (when $P(x, y, 0)$ coincides with $(0, 0, 0)$):

$$E_R = jC_0 R_i \sin\theta_i \frac{e^{-j2kR}}{8\pi R} \tag{1}$$

where $C_0 = \eta_0 \Delta l \omega I(\omega)/c$ is the dipole coefficient for antenna of length Δl carrying a current I whose radian frequency is ω and wavenumber is k in free space where the intrinsic impedance is η_0, R is the range between the ionospheric irregularities and radar, and $R_i(x, y)$ is the IRC at horizontal position (x, y) of the ionospheric scattering point, which may be considered as a random process that can be written in Fourier form:

$$R_i(x, y) = \sum_{\vec{K}_i} P_{\vec{K}_i} e^{j\vec{K}_i \cdot \vec{\rho}_i} \tag{2}$$

where $P_{\vec{K}_i}$ is the Fourier coefficient of the ionospheric irregularities, ρ_i is the diameter of the scattering area varied from 0 to $\Delta\rho_i$, and $\vec{K}_i$ is the wavenumber of the ionospheric irregularities. The field in (1) can be transformed to the time domain by applying inverse Fourier transform (see (7) in [18]):

$$E_R(t) = \frac{\sin\theta_i}{4\pi^2 R \Delta\rho_i^2} \left[\mathcal{F}_t^{-1}(jC_0) \overset{t}{*} \delta\left(t - \frac{2R}{C}\right)\right] \sum_{\vec{K}_i} P_{\vec{K}_i} \cdot \int_0^{\Delta\rho_i} J_0(K_i\rho_i)\, \rho_i d\rho_i \tag{3}$$

where $J_0(K_i\rho_i)$ is zero-order Bessel function, $\mathcal{F}_t^{-1}$ denotes inverse Fourier transform, $\overset{t}{*}$ denotes time convolution, and $\delta(\cdot)$ is the Dirac delta function.

2.1. The Electric Field for FMCW Waveform. The time domain expression for the FMCW transmitting antenna current waveform within one sweep interval is given as

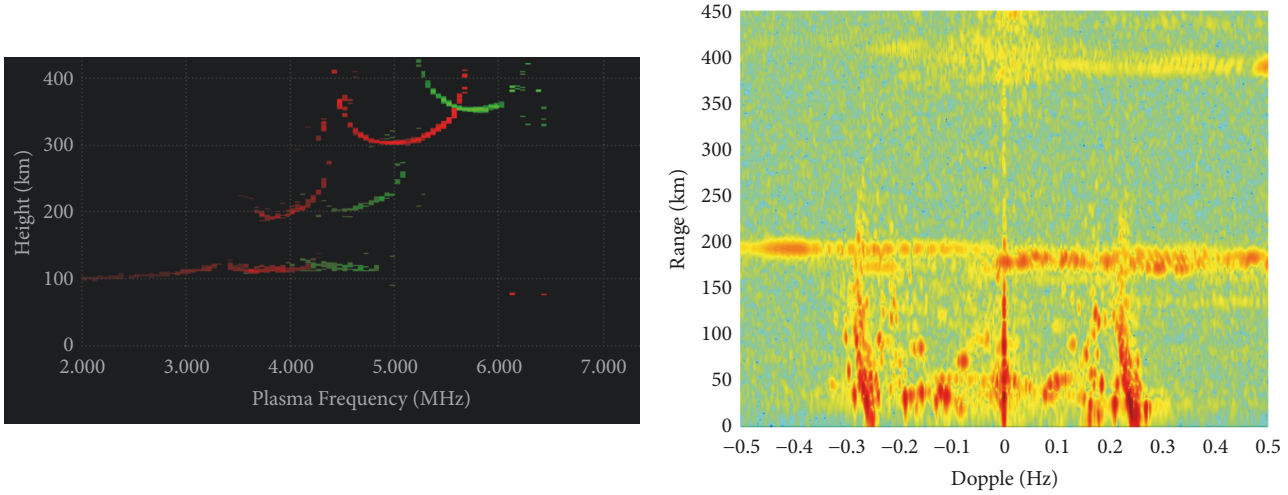

(a) (b)

Figure 2: The comparison of ionogram and RD spectrum on 10:53 am, June 28, 2018, location: Weihai (37.5°N, 122°E), China. (a) Ionogram (the horizontal axis is the plasma frequency and the vertical axis is the virtual height). (b) RD spectrum.

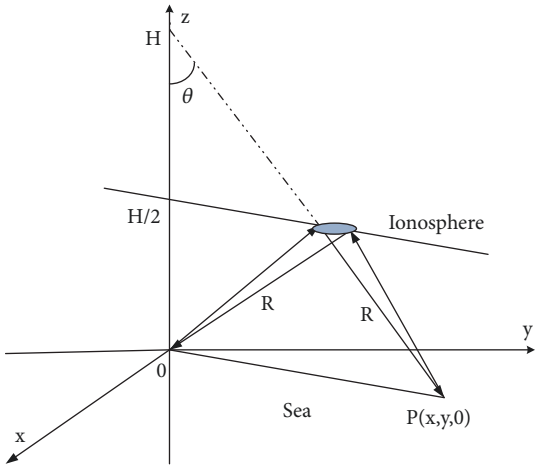

Figure 3: Scattering geometry for ionospheric backscattering.

$$i(t) = I_0 e^{j(\omega_0 t + \alpha\pi t^2)} \left[h\left(t + \frac{T_r}{2}\right) - h\left(t - \frac{T_r}{2}\right) \right] \quad (4)$$

where I_0 is the peak current, ω_0 is the radian frequency, $\alpha = B/T_r$ is the frequency sweep rate, B is the sweep bandwidth, T_r is the sweep interval, and $h(t)$ is the Heaviside function. Unlike pulsed radar, the range method for FMCW radar is to use the differential frequency between the transmitting and receiving signal:

$$R = \frac{c\Delta f}{2\alpha} = \frac{c\left|f_t - f_r\right|}{2\alpha} \quad (5)$$

where R is the target range, c is the light speed, and f_t and f_r are the frequencies of transmitting and receiving signal, respectively.

For dipole antenna transmitting FMCW signal, we have the approximate expression in the derivative:

$$\begin{aligned} \mathscr{F}_t^{-1}(jC_0) &= \frac{\eta_0 \Delta l}{c} \frac{di(t)}{dt} \\ &\approx jk_0\eta_0 \Delta l I_0 e^{j(\omega_0 t + \alpha\pi t^2)} \left[h\left(t + \frac{T_r}{2}\right) - h\left(t - \frac{T_r}{2}\right) \right] \end{aligned} \quad (6)$$

where $k_0 = \omega_0/c$. Then (3) becomes

$$\begin{aligned} E_R(t) = {} & \frac{jk_0\eta_0 \Delta l I_0 \sin\theta_i}{4\pi^2 R \Delta\rho_i^2} \sum_{\vec{K}_i} P_{\vec{K}_i} \int_0^{\Delta\rho_i} J_0(K_i\rho_i)\,\rho_i d\rho_i \\ & \times e^{j\omega_0(t-2R/c)} e^{j\alpha\pi(t-2R/c)^2} \left[h\left(t + \frac{T_r}{2} - \frac{2R}{c}\right) \right. \\ & \left. - h\left(t - \frac{T_r}{2} - \frac{2R}{c}\right) \right] \end{aligned} \quad (7)$$

After the demodulation processing, (7) reduces to

$$\begin{aligned} E_R^D(t) = {} & \frac{jk_0\eta_0 \Delta l I_0 \sin\theta_i}{4\pi^2 R \Delta\rho_i^2} \sum_{\vec{K}_i} P_{\vec{K}_i} \int_0^{\Delta\rho_i} J_0(K_i\rho_i)\,\rho_i d\rho_i \\ & \times e^{-j(4\pi\alpha R^2/c^2 - 2k_0 R)} e^{j(4\pi\alpha R/c)t} \left[h\left(t + \frac{T_r}{2} - \frac{2R}{c}\right) \right. \\ & \left. - h\left(t - \frac{T_r}{2} - \frac{2R}{c}\right) \right] \end{aligned} \quad (8)$$

where the superscript D represents demodulation.

For FMCW, the target range is determined by the difference frequency of the demodulated electric field. Thus the range transform involves Fourier transform the electric field with respect to t for obtaining the difference frequency.

Only the last two terms are function of t and their Fourier transforms are

$$\begin{aligned}\mathcal{F}&\left\{e^{j(4\pi\alpha R/c)t}\left[h\left(t+\frac{T_r}{2}-\frac{2R}{c}\right)\right.\right.\\&\left.\left.-h\left(t-\frac{T_r}{2}-\frac{2R}{c}\right)\right]\right\}=\int_{2R/c-T_r/2}^{2R/c+T_r/2}e^{j(4\pi\alpha R/c)t}\\&\cdot e^{-j\omega t}dt=T_r e^{j(4\pi\alpha R/c-\omega)(2R/c)}Sa\left[\frac{T_r}{2}\left(\omega\right.\right.\\&\left.\left.-\frac{4\pi\alpha R}{c}\right)\right]\end{aligned}\tag{9}$$

Inserting (9) into (8), the frequency domain expression for FMCW can be obtained:

$$\begin{aligned}E_R^D(\omega_r)&=\mathcal{F}\left\{E_R^D(t)\right\}\\&=\frac{jk_0\eta_0\Delta lI_0\sin\theta_i T_r}{4\pi^2R\Delta\rho_i^2}\sum_{\vec{K}_i}P_{\vec{K}_i}\int_0^{\Delta\rho_i}J_0\left(K_i\rho_i\right)\rho_i d\rho_i\\&\times e^{-j2(k_0+\omega_r/c)R}e^{j(4\pi\alpha R^2/c^2)}Sa\left[\frac{T_r}{2}\left(\omega_r-\frac{4\pi\alpha R}{c}\right)\right]\end{aligned}\tag{10}$$

Here, ω has been renamed as ω_r and $Sa(x)$ is the sampling function of $\sin(x)/x$. For a given frequency ω_r, there is a corresponding delay time Δt which is the total delay between the ionospheric irregularities and radar. Then the apparent ionosphere reflection range R_0 and range resolution ΔR can be defined as

$$\begin{aligned}R_0&=\frac{c\Delta t}{2}=\frac{c\omega_r}{4\pi\alpha},\\\Delta R&=\frac{c}{2B}\end{aligned}\tag{11}$$

And we define

$$\begin{aligned}k_B&=\frac{2\pi B}{c},\\k_r&=\frac{\omega_r}{c},\\R'&=R_0-R\end{aligned}\tag{12}$$

Thus the variable of the sampling function in (10) becomes

$$\frac{T_r}{2}\left(\omega_r-\frac{4\pi\alpha R}{c}\right)=\frac{2\pi B}{c}\left(R_0-R\right)=k_BR'\tag{13}$$

Suppose that the sampling function is narrow band and most of the values are from the ranges in the neighborhood of peak, which means those values of R' satisfied $|k_BR'|<\pi/2$. The characteristic of the sampling function Sa implies some range-bin to range-bin interaction, which can be regarded as the varying parameterΔr. When $\Delta r=\Delta R/2$, it means there is no interaction between the radar range bins. The effect of range bins interaction may be written as

$$\Delta r=\frac{\Delta R}{2},\Delta R,\cdots\frac{k\Delta R}{2}\cdots,\quad k=1,2,\cdots\tag{14}$$

Due to random variable $R'\in[-\Delta r,\Delta r]$, the interval of k_BR' is $[-k\pi/2,k\pi/2]$. Suppose that R' is have a uniform distribution, then the expectation of Sa function is given by

$$\begin{aligned}E\left\{Sa\left(k_BR'\right)\right\}&=\frac{\int_{-\Delta r}^{\Delta r}Sa\left(k_BR'\right)dR'}{2\Delta r}=\frac{Si\left(k\pi/2\right)}{\pi}\\&\approx\frac{1}{k}\end{aligned}\tag{15}$$

where $Si(x)=\int_0^x(\sin t/t)dt$. Thus the received electric field equation for FMCW radar can be derived from (10) as

$$\begin{aligned}E_R^D(\omega_r)&=\frac{jk_0\eta_0\Delta lI_0\sin\theta_i T_r}{4\pi^2R_0\Delta\rho_i^2}\\&\cdot e^{-j2(k_0+k_r)R}e^{j(4\pi\alpha R^2/c^2)}\sum_{\vec{K}_i}P_{\vec{K}_i}\\&\cdot\int_0^{\Delta\rho_i}J_0\left(K_i\rho_i\right)\rho_i d\rho_i\times Sa\left(k_BR'\right)\end{aligned}\tag{16}$$

Comparing with the electric field for pulsed radar ((9) in [18]), we can find that the main difference is the Sa function, which is determined by the range bins interaction parameter k. This term makes the amplitude of ionospheric clutter of FMCW radar lower than pulsed radar.

2.2. Vertical Received Power for FMCW. In reality, the ionosphere has a slow time variation. Thus $R_i(x,y)$ in (2) should be modified as

$$R_i(x,y,t)=\sum_{\vec{K}_i,\omega_i}P_{\vec{K}_i,\omega_i}e^{j(\vec{K}_i\cdot\vec{\rho}_i+\omega_it)}\tag{17}$$

where ω_i is the frequency of the ionospheric irregularities. Supposing ω_i is small enough that time variation during a single sweep can be negligible. Therefore, only sweep to sweep variations are considered. Assuming that $R_i(x,y,t)$ is a stationary, homogeneous random process, it is useful to investigate the statistical characteristics of the received electric field by its autocorrelation function as

$$\begin{aligned}R(\tau)&=\frac{A_r}{2\eta_0}\frac{1}{T_r^2}\left\langle E(t+\tau)E^*(t)\right\rangle\\&=\frac{A_r\eta_0k_0^2\Delta l^2I_0^2\sin^2\theta_i}{32\pi^4{R_0}^2\Delta\rho_i^4}\int_{\vec{K}_i}\int_{\omega_i}S_{R_i}\left(\vec{K}_i,\omega_i\right)\\&\cdot\left|\int_0^{\Delta\rho_i}J_0\left(K_i\rho_i\right)\rho_i d\rho_i\right|^2Sa^2\left(k_BR'\right)e^{j\omega_i\tau}d\vec{K}_id\omega_i\end{aligned}\tag{18}$$

where A_r is the receiving antenna effective area. $*$ represents complex conjugation, and $S_{R_i}(\vec{K}_i,\omega_i)$ is the spectral density of

the ionospheric irregularities which has the wave vector $\vec{K}_i$ and frequency ω_i. The Fourier transform of autocorrelation function $R(\tau)$ gives the power spectral density (PSD) as

$$P(\omega_d) = \mathcal{F}\{R(\tau)\} = \frac{A_r \eta_0 k_0^2 \Delta l^2 I_0^2 \sin^2\theta_i}{32\pi^4 {R_0}^2 \Delta\rho_i^4} \int_{\vec{K}_i} \int_{\omega_i} S_{R_i} \cdot \left(\vec{K}_i, \omega_i\right) \times \left| \int_0^{\Delta\rho_i} J_0\left(K_i\rho_i\right) \rho_i d\rho_i \right|^2 Sa^2\left(k_B R'\right) \cdot \delta\left(\omega_d - \omega_i\right) d\vec{K}_i d\omega_i \quad (19)$$

where ω_d is the observed Doppler frequency.

Combining the layered ionosphere model proposed in [18] with the vertical ionospheric model of the phase spectrum in [15], $S_{R_i}(\vec{K}_i, \omega_i)$ can be expressed as

$$S_{R_i}\left(\vec{K}_i, \omega_i\right) = k_0 \left(1 + \frac{4 z_0 r_e^2 \lambda_0^2}{k_0} \log \frac{z_0}{z_0 - z_0'} \cdot \frac{8\pi^3 \kappa_0 \left\langle N_{e1}^2 \right\rangle \delta\left(\kappa_y\right) \delta\left(\omega_i - \kappa_x v_h - 2k_0 v_v\right)}{\left(\kappa_0^2 + {\kappa_x}^2\right)^{3/2}} + \cdots \right) \quad (20)$$

where z_0 is the ionosphere thickness, z_0' is the height of below z_0 on the order of one radar wavelength, r_e is the classical electron radius, λ_0 is the wavelength of radar, κ_x and κ_y are the horizontal components of the density irregularities wave number κ, with x being the east coordinate and y being the north coordinate in geomagnetic coordinate system, $\kappa_0 \approx 10^{-4}\mathrm{m}^{-1}$ is the "outer" scale length parameter, $\langle N_{e1}^2 \rangle$ is the variance of the electron density fluctuations at the reflection height, and v_h and v_v are the horizontal and vertical ionospheric plasma drift velocities.

Finally, the vertical received PSD for FMCW from (19) is reduced to

$$P_v(\omega_r, \omega_d) = \frac{k_0^3 \eta_0 \Delta l^2 I_0^2 A_r \sin^2\delta\theta}{32\pi^4 R_0^2 \Delta\rho_i^4} Sa^2\left(k_B R'\right) \cdot \left| \int_0^{\Delta\rho_i} J_0\left(\frac{\omega_d - 2k_0 v_v}{v_h} \rho_i \right) \rho_i d\rho_i \right|^2 \times \left(1 + \frac{4 z_0 r_e^2 \lambda_0^2}{k_0} \cdot \log \frac{z_0}{z_0 - z_0'} \frac{8\pi^3 \kappa_0 \left\langle N_{e1}^2 \right\rangle}{\left(\kappa_0^2 + \left(\left(\omega_d - 2k_0 v_v\right)/v_h\right)^2\right)^{3/2}} + \cdots \right) \quad (21)$$

3. Backscattering Received Power Spectrum for FMCW Source

The power spectrum of the HF signal phase backscattering from plasma structures in the auroral has been given in [15]. Assumptions are easily satisfied, such as the auroral magnetic field of the Earth which is approximately vertical to the surface, making the integral of phase autocorrelation function much simple. However, most of HFSWRs are located at mid-latitude. Therefore the magnetic field of the HFSWR location dissatisfies those conditions. Here, we rotate the coordinate axis twice, making the x-axis point to the east of geomagnetic field to eliminate the x component and making the z-axis coinciding with the local magnetic field **B** to eliminate z component. Then the integral of the autocorrelation function only leaves the integral about y. The following is the mathematical modeling process.

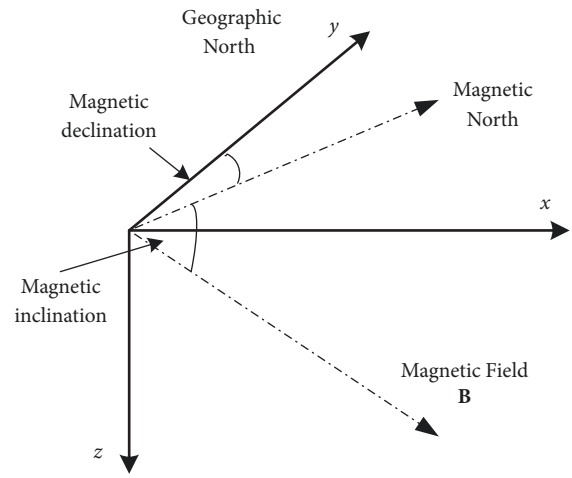

Figure 4: Scattering geometry for ionospheric backscattering.

It is assumed that α_D and α_I are the magnetic declination and magnetic inclination, respectively (see Figure 4). The coordinate of ray trajectory is $X_1 = (x_1, y_1, z_1)$ in the geographic coordinate system, with x_1 east, y_1 north, and z_1 vertical. Now fixing z_1-axis, we rotate x_1 and y_1 axis α_D degrees, such that x_2 points to magnetic east and y_2 points to magnetic north. The magnetic field lies in the y_2-z_2 plane. The magnetic coordinate system is denoted by X_2:

$$X_2 = \begin{pmatrix} \cos\alpha_D & \sin\alpha_D & 0 \\ -\sin\alpha_D & \cos\alpha_D & 0 \\ 0 & 0 & 1 \end{pmatrix} X_1 \quad (22)$$

Then we fixed x_2-axis, and rotated y_2 and z_2 axis $\pi/2 - \alpha_I$ degrees, such that z_2 coincides with magnetic field **B**. The new coordinate system is denoted by X_3:

$$X_3 = \begin{pmatrix} 1 & 0 & 0 \\ 0 & \sin\alpha_I & \cos\alpha_I \\ 0 & -\cos\alpha_I & \sin\alpha_I \end{pmatrix} X_2 \quad (23)$$

Thus the Y component in X_3 coordinate system can be expressed as

$$y_3 = -\sin\alpha_I \sin\alpha_D x_1 + \sin\alpha_I \cos\alpha_D y_1 + \cos\alpha_I z_1 \quad (24)$$

The horizontal distance L traveled in the ionosphere is given by

$$\begin{aligned} L &= \left|y_3 - y_3'\right| \\ &= -\sin\alpha_I \sin\alpha_D \left|x_1 - x_1'\right| + \sin\alpha_I \cos\alpha_D \left|y_1 - y_1'\right| \\ &\quad + \cos\alpha_I \left|z_1 - z_1'\right| \end{aligned} \tag{25}$$

where (x_1, y_1, z_1), (x_1', y_1', z_1') are the locations where the radar signal enters the ionosphere and backscattering takes place, respectively. In the auroral zone, $\alpha_D = 0$, $\alpha_I = \pi/2$, then (25) becomes

$$L = \left|y_1 - y_1'\right| \tag{26}$$

Therefore this is a special case of (25). Next, we estimate the scope of L. The ray trajectory has an inverted parabola form within the ionosphere (see (31) in [15]):

$$\frac{z}{z_0} = -\frac{1}{4}\csc^2\theta \left(\frac{\rho}{z_0}\right)^2 + \cos^2\theta \tag{27}$$

where θ is the elevation angle with respect to zenith; ρ is the radial range in the x-y plane. The point $(x, y) = (0, 0)$ is the peak of the parabolic trajectory. At this point, we have

$$z = z_0 \cos^2\theta \tag{28}$$

The radar pulse obliquely incident on the ionosphere at z=0, then (27) gives

$$\rho = z_0 \sin 2\theta \tag{29}$$

From (24), (28), and (29), the scope of L can be expressed as

$$\begin{aligned} &0 \le L \\ &\le z_0 \left[\sin 2\theta \sin\alpha_I \left(\cos\alpha_D - \sin\alpha_D\right) + \cos^2\theta \cos\alpha_I\right] \end{aligned} \tag{30}$$

Thus the approximate expression of the oblique backscattering phase spectrum in mid-latitude can be written as

$$\begin{aligned} S_{\varphi 1}\left(\kappa_x, \kappa_y, \omega\right) &= 32\pi^3 \kappa_0 z_0 \left(r_e \lambda \csc\theta\right)^2 \left\langle N_{e1}^2 \right\rangle \delta\left(\kappa_y\right) \\ &\cdot \delta\left(\omega - \kappa_x v_{dx} - 2k_0 v_{dy}\right) \\ &\times \frac{\left[\sin 2\theta \sin\alpha_I \left(\cos\alpha_D - \sin\alpha_D\right) + \cos^2\theta \cos\alpha_I\right]}{\left(\kappa_0^2 + \kappa_x^2\right)^{3/2}} \end{aligned} \tag{31}$$

where v_{dx} is the plasma drift velocity which is perpendicular to the radar beam in azimuthal direction; v_{dy} is the plasma drift velocity along the radar beam in azimuthal direction. Due to the scattering geometry, the plasma drift velocities can be represented as

$$v_{dx} = v_h \cos\theta + v_v \sin\theta \tag{32}$$

$$v_{dy} = v_h \sin\theta + v_v \cos\theta \tag{33}$$

Finally, using this specific ionosphere spectral density model, the expression of oblique PSD for FMCW in mid-latitude reduces to

$$\begin{aligned} P_o\left(\omega_r, \omega_d\right) = \frac{k_0^3 \eta_0 \Delta l^2 I_0^2 A_r \sin^2\theta}{32\pi^4 R_0^2 \Delta\rho_i^4} Sa^2\left(k_B R'\right) \left| \int_0^{\Delta\rho_i} J_0\left(\frac{\omega_d - 2k_0\left(v_h \sin\theta + v_v \cos\theta\right)}{v_h \cos\theta + v_v \sin\theta} \rho_i\right) \rho_i d\rho_i \right|^2 \\ \times \left(1 + \frac{32\pi^3 \kappa_0 \left(r_e \lambda_0 \csc\theta_i\right)^2 \left\langle N_{e1}^2 \right\rangle \left(\sin 2\theta \sin\alpha_I \left(\cos\alpha_D - \sin\alpha_D\right) + \cos^2\theta \cos\alpha_I\right)}{k_0 \left(\kappa_0^2 + \left(\left(\omega_d - 2k_0\left(v_h \sin\theta + v_v \cos\theta\right)\right) / \left(v_h \cos\theta + v_v \sin\theta\right)\right)^2\right)^{3/2}} + \cdots \right) \end{aligned} \tag{34}$$

4. Numerical Simulations and Experiment Results

4.1. Numerical Simulations. Firstly we simulate the expectation of the random function $Sa^2(k_B R')$, which is the main difference between the PSD of pulsed radar and FMCW radar, as shown in Figure 5. We can see that $Sa^2(k_B R')$ changed with the range bins interaction parameter k, which are roughly coincident with (15). When the range resolution ΔR is 5km (the sweep bandwidth is chosen as 30kHz), k=5 means the range bins interaction is 25km. The corresponding peak power of ionospheric clutter for FMCW waveform is lower than that of pulsed waveform about −7dB. As k increases, i.e., the radar signal is observed from increasingly larger ionospheric regions, the peak power of ionospheric clutter for FMWC waveform is reduced.

In order to study the intensity of the ionosphere clutter and the sea clutter, we use the normalized ionospheric clutter power function defined as the ratio of the ionospheric clutter power to the average first-order sea clutter power. The main parameters are listed in Table 1. The parameters are the same as those in [18], for the sake of comparison with pulsed waveform. Figure 6(a) shows the comparison results when FMCW parameters are with sweep bandwidth B= 30 kHz and k=10. It is observed that the peak power of FMCW is lower than that of pulsed waveform about −10dB. The power of the ionospheric clutter for FMCW exceeds the average sea clutter power by about 35dB. Moreover, the main-lobe

Table 1: Main parameters in the simulation.

Symbol	Quantity	Parameters
f_0	Radar frequency	4.1MHz
R_0	Ionosphere height	300km
$\Delta\rho_i$	Scattering region radius	2.5km
z_0	Ionosphere thickness	50km
r_e	Classical electron radius	2.8×10^{-15}m
v_h	Horizontal ionospheric plasma drift velocity	100m/s
$\langle N_{e1}^2 \rangle$	Variance of the electron density fluctuations	10^{18}m^{-6}
κ_0	Out scale length parameter	10^{-4}m^{-1}
k	range bins interaction parameter	10
B	sweep bandwidth	30kHz

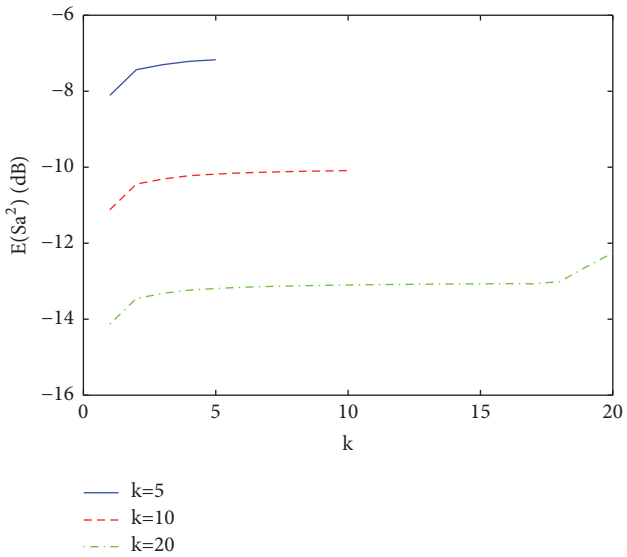

Figure 5: The expectation of function Sa^2 with parameter k.

spectral width of FMCW is obviously narrower than that of the pulsed waveform. Figure 6(b) illustrates the changes in the power of ionospheric clutter with the range bins interaction. We can see that the peak power increases when k decreases.

Figure 7(a) illustrates the PSD of ionospheric clutter for FMCW from oblique backscattering with different incidence angles from 30° to 60°, when the vertical ionospheric velocity v_v is set as -5m/s, 5m/s, 15m/s, respectively. The horizontal ionospheric velocity v_h is set as 50m/s. Magnetic declination is set as 55°, and magnetic inclination is set as -7°, which are the magnetic field of Weihai (38°N, 122°E), China. We can find that the vertical ionospheric motion not only results in a Doppler shift, but also changes the peak power. This is different from the case of vertical reflection [18], where the vertical ionospheric motion only causes Doppler shift. The peak power of the ionospheric clutter with $\theta = \pi/3$ exceeds that of $\theta = \pi/4$ nearly 17dB.

Figure 7(b) illustrates the horizontal distance in ionosphere with L denoting the magnetic inclination varied from 0° (the equator zone) to 90° (the auroral zone) on the incidence angles. It is observed that L changed not only with magnetic inclinations but also with incidence angles. The maximum distance between different latitudes can reach 30km.

Figure 8 shows the simulation of the oblique range-Doppler power spectrum for FMCW (background white noise has been added). The main parameters for the three regions are as follows: the ranges are set as 100-150km, 200-250km, and 250-300km, respectively; the incidence angles are set as 30°, 45°, and 60°, respectively; the patch radii are set as 0.5km, 1.5km, and 2.5km, respectively; the variance of the electron density fluctuations is set as 10^{16}m^{-6}, 10^{18}m^{-6}, and 10^{20}m^{-6}, respectively; the vertical ionospheric velocity v_v is set as -5m/s, -10m/s, and 5m/s, respectively; the ionospheric velocity of ionospheric velocity v_h is set as 50m/s, 75m/s, and 100m/s, respectively. The reason for setting these parameters sequentially is to make the peak power and Doppler bandwidth of ionospheric clutter expanding. The oscillating shapes of the power spectrum are caused by the integral over the zero-order Bessel function.

By changing each parameter while keeping other parameters invariant, the simulation results show some characteristics as follows: the Doppler frequency of the power peak is mainly determined by the along radar beam velocities; the Doppler bandwidth spreading is mainly determined by the patch radii and the ionospheric velocities of cross radar beam; the peak of power is mainly determined by the variance of electron density fluctuations, radar frequencies, ionosphere ranges, and incidence angles.

4.2. Experiment Results. The HFSWR and Ionosonde are located at Weihai (37.5°N, 122°E), where is on the edge of the Yellow Sea. Experiment has been processed on 10:55 am, June 20, 2018 (Beijing Time). The data of HFSWR are collected during the coherent integration time (CIT) from 10:55 to 11:00. The radar operating frequency is 6MHz, and the sweep bandwidth is 30 kHz. The ionogram is collected in one minute: 11:02. The ionogram is shown in Figure 9(a). It is observed that the critical frequency of E layer is about 5.5MHz, and the range spreads from 100km to 120km. Corresponding spreading in range can be found in Figure 9(b), where it is about 150-200km. This may be considered from the oblique backscattering for HFSWR. The extraordinary reflection in F layer is about 330-380km, which can also be found in RD spectrum. Because the locations of two figures are at a similar range, this may be considered as from the vertical reflection for HFSWR.

Due to lack of the actual power of sea clutter, we cannot testify the model precisely. However, we can get the distribution shapes of the ionospheric irregularities and the relative intensity of the received power. Figures 10(a) and 10(b) illustrate the inversion result of E layer and F layer, respectively.

The selected range of F layer is from 350km to 390km, and the selected Doppler width is from 0.08Hz to 0.23Hz. The F layer critical frequency is 6.3MHz, the corresponding maximum electron density is $4.9*10^{11}\text{m}^{-3}$. Therefore we set the average of the electron density fluctuation as $4.9*10^{9}\text{m}^{-3}$, which is 1% of the maximum electron density. The inversion result shows that the main Doppler peak of irregularities is

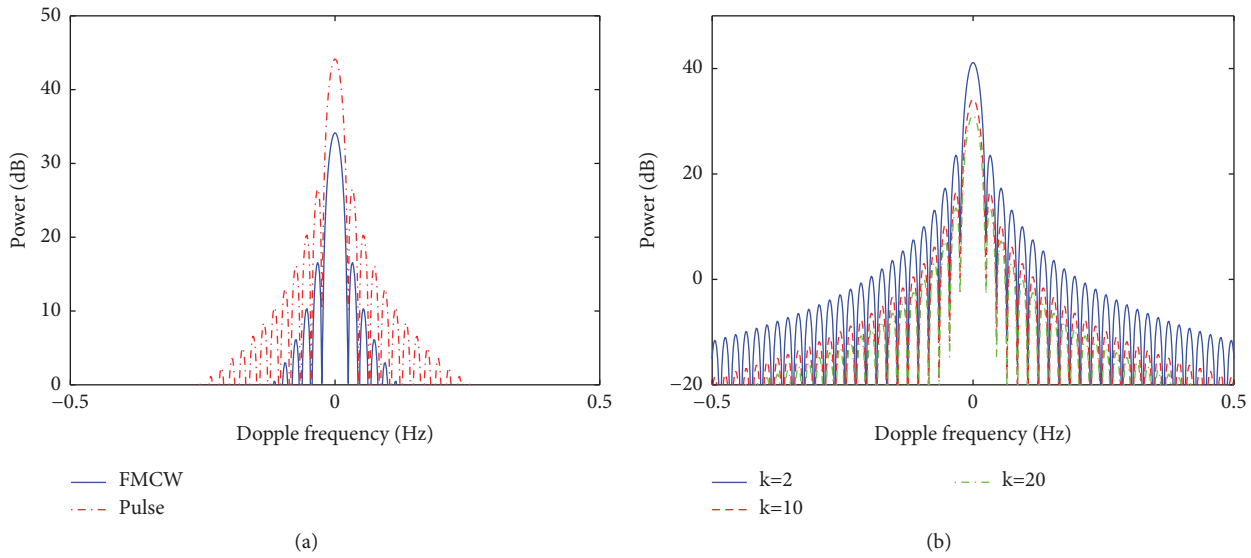

FIGURE 6: Simulations of vertical normalized ionospheric clutter power: (a) for the pulsed and FMCW waveforms and (b) with different k.

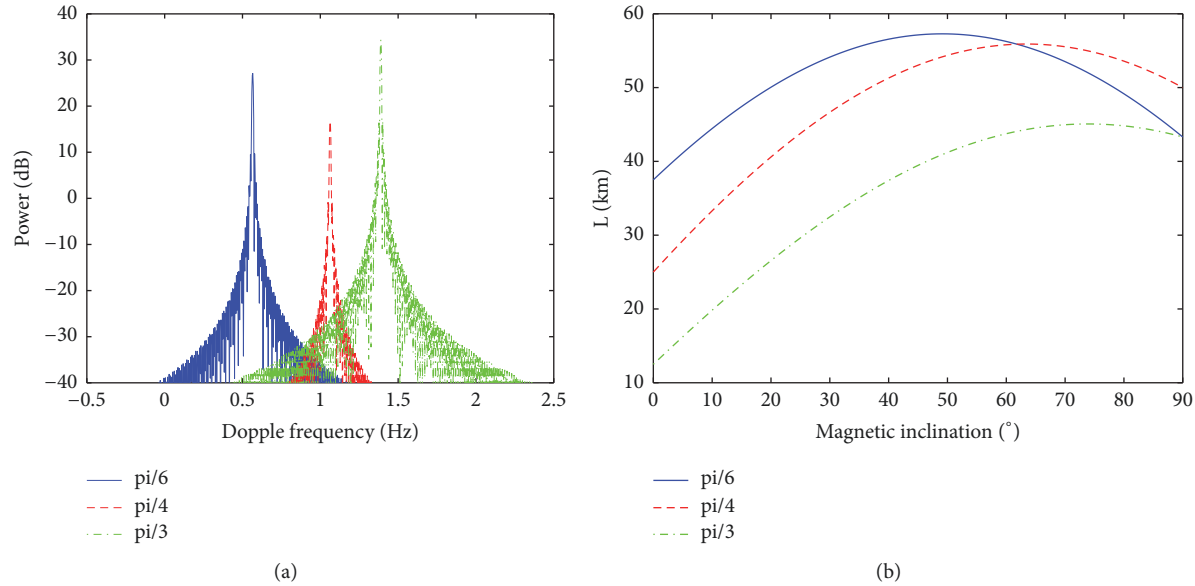

FIGURE 7: Simulations of oblique backscattering: (a) power with different incidence angles for FMCW. (b) L with different incidence angles.

0.1657Hz, which means the vertical drift velocities of the most fluctuation irregularities is about 4.14m/s. The main peak of irregularities in range distribution is 369km. Noted that the Doppler distribution is stratified and the oscillating shapes, which are consistent with Figure 8.

The selected range of E layer is from 160km to 210km, and the selected Doppler width is from -0.5Hz to 0.5Hz. The E layer critical frequency is 5.5MHz, the corresponding maximum electron density is $3.7*10^{11}\mathrm{m}^{-3}$. From the figure, we can see that the main peak of irregularities in range distribution is 198km. The range spreading, which should come from multipath reflection, also accords with RD spectrum in Figure 9(b). The peak Doppler is -0.265Hz, which implies the vertical drift velocities of the irregularities is about -6.625m/s. The average of the electron density fluctuation is about $3.9*10^{9}\mathrm{m}^{-3}$, which is almost 10% of the E layer maximum electron density. From Figure 10, the irregularities within ionosphere shows more Doppler characteristics, which means the drift motion of irregularities has a significant influence on ionospheric clutter.

5. Conclusions

This paper has developed an ionospheric clutter model for the vertical and backscatter reflection with FMCW source. The theory contained the development of the electric field equations and the derivation of the power spectrum for ionospheric clutter. The main difference of PSD between

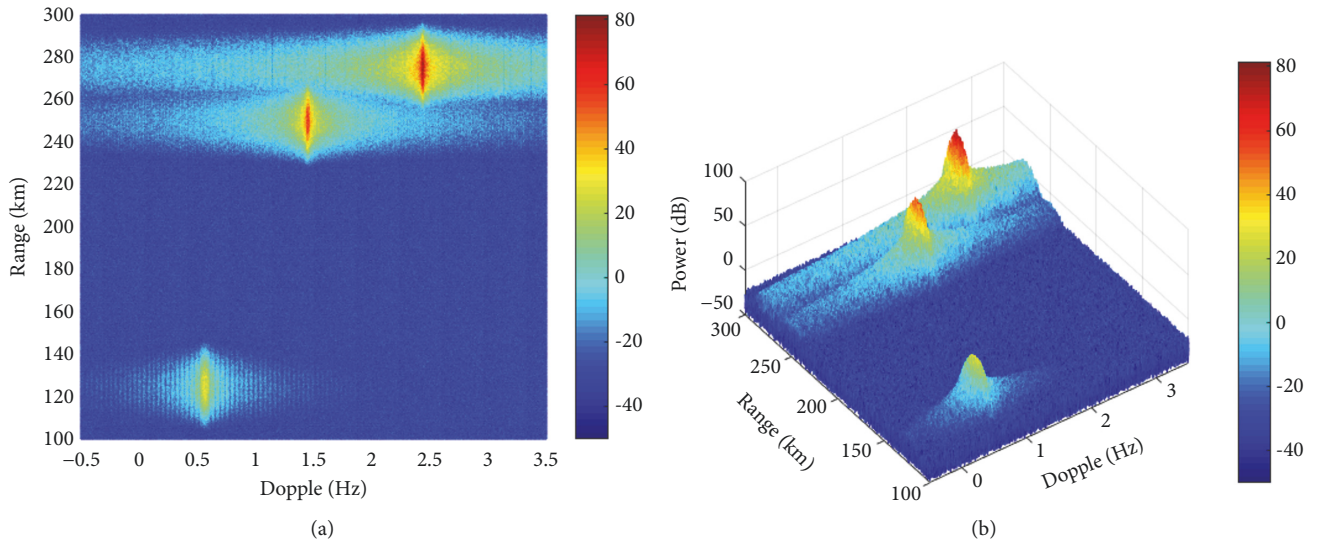

Figure 8: Simulated oblique backscattering PSD of ionospheric clutter: (a) R-D spectrum. (b) 3D spectrum.

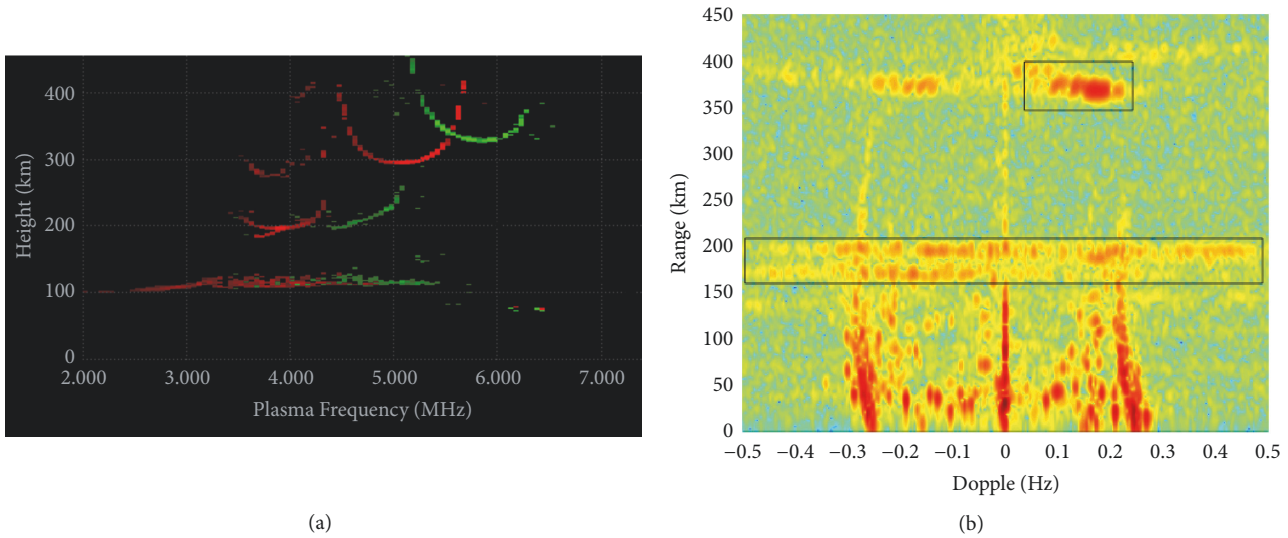

Figure 9: The comparison of Ionogram and RD spectrum of HFSWR on 10:55 am, June 28, 2018 (Beijing Time), location: Weihai (37.5°N, 122°E): (a) Ionogram; (b) RD spectrum.

FMCW and pulsed waveform is the Sa function, which makes the peak power of FMCW in average lower than pulsed waveform, and the Doppler bandwidth of FMCW is much narrower than that of the pulsed waveform. The generalized power spectrum for backscatter sky-wave propagation (0.5 jumps) in mid-latitude was also derived.

Numerical simulations illustrated that the Doppler bandwidth was spreading and the peak was heightening with the elevation angle increases. The 2D and 3D of RD spectrum were also simulated. At last, we processed the measured HFSWR data and inversed the variance of the electron density fluctuation and the vertical velocity of the irregularities within ionosphere by the Ionosonde data. Such researches could be beneficial to the better understanding of the characteristic of ionospheric clutter and suppressing ionospheric clutter techniques for HFSWR.

Data Availability

For the radar measured date, we will be very happy to share with you; however, at the present, for the confidentiality issues and the security concerns, it is not allowed to be open and to provide the data availability statement.

Conflicts of Interest

The authors declare no conflicts of interest.

Acknowledgments

Thanks are due to the Key Laboratory of Marine Environmental Monitoring and Information Processing, Harbin Institute of Technology, China, for data support. This research

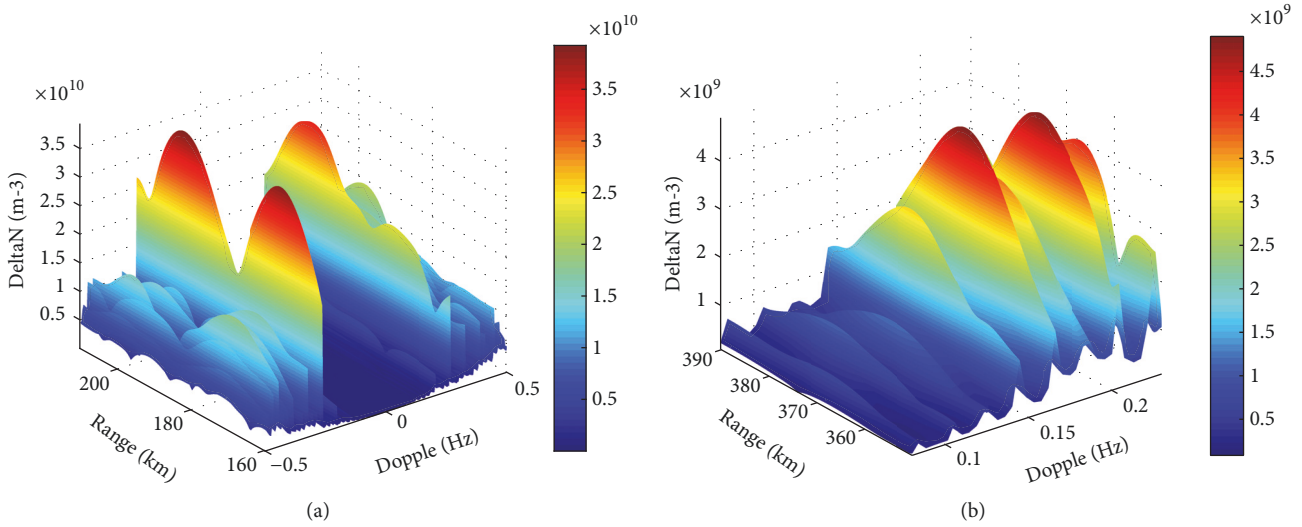

Figure 10: Experimental inversion results: (a) E layer; (b) F layer.

was funded by the National Natural Science Foundations of China, Grants nos. 61801141, 61571157, and 61571159.

References

[1] L. Sevgi, A. Ponsford, and H. C. Chan, "An integrated maritime surveillance system based on high-frequency surface-wave radars. 1. Theoretical background and numerical simulations," *IEEE Antennas and Propagation Magazine*, vol. 43, no. 4, pp. 27–43, 2001.

[2] X. Yang, C. Yu, A. Liu, L. Wang, and T. Quan, "The vertical ionosphere parameters inversion for high frequency surface wave radar," *International Journal of Antennas and Propagation*, vol. 2016, Article ID 8609372, pp. 1–8, 2016.

[3] H. C. Chan, "Characterization of ionospheric clutter in HF surface wave radar," *Defense Research and Development Canada - Ottawa*, vol. 114, pp. 1–110, 2003.

[4] T. Thayaparan and J. MacDougall, "Evaluation of ionospheric sporadic-E clutter in an arctic environment for the assessment of high-frequency surface-wave radar surveillance," *IEEE Transactions on Geoscience and Remote Sensing*, vol. 43, no. 5, pp. 1180–1188, 2005.

[5] F. Jangal, S. Saillant, and M. Hélier, "Ionospheric clutter mitigation using one-dimensional or two-dimensional wavelet processing," *IET Radar, Sonar & Navigation*, vol. 3, no. 2, pp. 112–121, 2009.

[6] X. Guo, H. Sun, and T. S. Yeo, "Interference cancellation for high-frequency surface wave radar," *IEEE Transactions on Geoscience and Remote Sensing*, vol. 46, no. 7, pp. 1879–1891, 2008.

[7] X. Zhang, Q. Yang, and W. Deng, "Weak target detection within the nonhomogeneous ionospheric clutter background of HFSWR based on STAP," *International Journal of Antennas and Propagation*, vol. 2013, Article ID 382516, 11 pages, 2013.

[8] D. Yao, X. Zhang, Q. Yang, and W. Deng, "Radio and clutter suppression algorithm based on spatial multiple beams for small-aperture HFSWR," *International Journal of Antennas and Propagation*, vol. 2018, 15 pages, 2018.

[9] H. Zhou, B. Wen, and S. Wu, "Ionospheric clutter suppression in HFSWR using multilayer crossed-loop antennas," *IEEE Geoscience and Remote Sensing Letters*, vol. 11, no. 2, pp. 429–433, 2014.

[10] X. Wan, C. Feng, and K. Hengyu, "Experimental trials on ionospheric clutter suppression for high-frequency surface wave radar," *IEE Proceedings Radar, Sonar and Navigation*, vol. 153, no. 1, pp. 23–29, 2006.

[11] X. Mao, H. Hong, W. Deng, and Y. Liu, "Research on polarization cancellation of nonstationary ionosphere clutter in HF radar system," *International Journal of Antennas and Propagation*, vol. 2015, 12 pages, 2015.

[12] J. Walsh and E. W. Gill, "An analysis of the scattering of high-frequency electromagnetic radiation from rough surfaces with application to pulse radar operating in backscatter mode," *Radio Science*, vol. 35, no. 6, pp. 1337–1359, 2000.

[13] J. Walsh, E. W. Gill, W. Huang, and S. Chen, "On the development of a high-frequency radar cross section model for mixed path ionosphere-ocean propagation," *Institute of Electrical and Electronics Engineers. Transactions on Antennas and Propagation*, vol. 63, no. 6, pp. 2655–2664, 2015.

[14] J. Walsh, J. Zhang, and E. W. Gill, "High-frequency radar cross section of the ocean surface for an FMCW waveform," *IEEE Journal of Oceanic Engineering*, vol. 36, no. 4, pp. 615–626, 2011.

[15] M. Ravan, R. J. Riddolls, and R. S. Adve, "Ionospheric and auroral clutter models for HF surface wave and over-the-horizon radar systems," *Radio Science*, vol. 47, no. 3, pp. 2655–2664, 2012.

[16] S. Chen, E. W. Gill, and W. Huang, "A first-order HF radar cross-section model for mixed-path ionosphere-ocean propagation with an FMCW source," *IEEE Journal of Oceanic Engineering*, vol. 41, no. 4, pp. 982–992, 2016.

[17] S. Chen, E. W. Gill, and W. Huang, "A high-frequency surface wave radar ionospheric clutter model for mixed-path propagation with the second-order sea scattering," *IEEE Transactions on Antennas and Propagation*, vol. 64, no. 12, pp. 5373–5381, 2016.

[18] S. Chen, W. Huang, and E. W. Gill, "A vertical reflection ionospheric clutter model for HF radar used in coastal remote sensing," *IEEE Antennas and Wireless Propagation Letters*, vol. 14, no. 99, pp. 1689–1693, 2015.